Three-Dimensional Chiral Active Ornstein-Uhlenbeck Model for Helical Motion of Microorganisms

Leon Lettermann[1,2] Falko Ziebert[1,2] Mirko Singer[3] Friedrich Frischknecht[3,4] and Ulrich S. Schwarz[1,2,*]

[1]*Institute for Theoretical Physics, Heidelberg University, Philosophenweg 19, 69120 Heidelberg, Germany*
[2]*Bioquant-Center, Heidelberg University, Im Neuenheimer Feld 267, 69120 Heidelberg, Germany*
[3]*Parasitology, Center for Infectious Diseases, Heidelberg University, Im Neuenheimer Feld 344, 69120 Heidelberg, Germany*
[4]*German Center for Infection Research (DZIF), Partner Site Heidelberg, 69120 Heidelberg, Germany*

Active movement is essential for the survival of microorganisms like bacteria, algae, and unicellular parasites. In three dimensions, both swimming and gliding microorganisms often exhibit helical trajectories. One such case are malaria parasites gliding through 3D hydrogels, for which we find that the internal correlation time for the stochastic process generating propulsion is similar to the time taken for one helical turn. Motivated by this experimental finding, here we theoretically analyze the case of finite internal correlation time for microorganisms with helical trajectories as chiral active particles with an Ornstein-Uhlenbeck process for torque. We present an analytical solution which is in very good agreement with computer simulations. We then show that, for this type of internal noise, chirality and rotation increase the persistence of motion and results in helical trajectories that have a larger long-time mean squared displacement than straight trajectories at the same propulsion speed. Finally, we provide experimental evidence for this prediction for the case of malaria parasites.

The survival of microorganisms like bacteria or algae is tightly connected to their ability to actively move, which is essential to seek out more favorable conditions, e.g., places which offer more nutrients or sunlight for photosynthesis [1,2]. Although sometimes movement is collective, e.g., in biofilms or during swarming, at the heart of all migration processes is always the capability of single microorganisms to internally generate forces and torques [3–5]. Migration over large distances is also essential for unicellular eukaryotes that have specialized in infecting mammalian hosts, such as the causative agents of the diseases malaria or toxoplasmosis [6]. Interestingly, in three dimensions many microorganisms exhibit helical trajectories [7,8]. This includes species of swimming bacteria [9,10], swimming algae [11–13], and gliding parasites [14–16]. In Fig. 1(a), we show the helical trajectories of malaria parasites gliding through 3D synthetic hydrogels (see Appendix A for details).

Since the pioneering work of Berg and Purcell, it is well accepted that one of the main challenges for moving microorganisms is to counter the effects of stochastic noise [17,18]. For example, the bacterium *Escherichia coli* uses a run-and-tumble strategy to move up and down chemotactic gradients; run times are typically of the order of one second, because for longer times orientation is lost due to rotational diffusion which results from collisions with

solvent molecules [19]. The interplay of self-propulsion and such external noise can be analyzed by the theory of active Brownian particles, which combines a constant propulsion force with stochastic noise for translation and rotation [20–23]. The active Brownian particle model has been used and extended in various contexts [24–29], including adding torques to obtain circle swimmers [30–36] and studying the influence of time-correlated noise [37–42].

However, most of these studies considered 2D cases, whereas helical motion of chiral active particles occurs in 3D [27]. If chiral active motion in 3D was analyzed theoretically, then it was mostly in the context of swimming. An early work on asymmetric swimmers in 3D
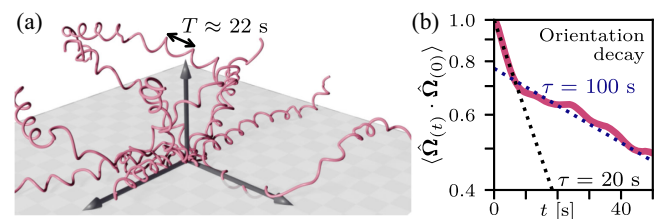

FIG. 1. (a) Reconstructed trajectories of malaria parasites gliding through synthetic hydrogels. Because this environment is nearly isotropic, the right-handed helical trajectories persist for long times. The typical turning time T is 22 s as indicated. (b) The direction of the angular velocity $\hat{\mathbf{\Omega}}$ displays a decay of autocorrelation with a fast ($\tau = 20$ s) and a slow ($\tau = 100$ s) regime (see Fig. 7 for a version with more details).

*Contact author: schwarz@thphys.uni-heidelberg.de

128403-1

considered the analogy to polymer models to extract new power laws for effective diffusion [43]; in general, the statistics of fluctuating helices is also an important aspect of helical biopolymers like DNA [44]. Previous work on sperm swimming considered stochasticity on the level of curvature and torsion and showed that helical trajectories are useful search strategies for chemotaxis in noisy environments [45,46]. This line of work also considered colored noise in the form of a power spectrum [46]. One study of chiral motion in 3D started from the full mobility tensor for an arbitrarily shaped particle and showed that helical trajectories are the most likely outcome [47]. Similarly, a chiral active Brownian particle model has been used to describe the helical motion of colonial choanoflagellates and to show that purely stochastic propulsion can result in effective dispersion [48]. Very recently, it has been shown in a deterministic model for sperm swimming that an asymmetric beat of the flagellum leads to helical trajectories with high persistence [49]. Collectively, this body of work demonstrates that helical trajectories can have evolutionary advantages for microorganisms.

Noise arises not only from the interaction of the microorganisms with their thermal environment, but also from the internal force-generating processes, which might have a correlation time on the same scale as the movement that they generate [38]. To address this aspect of the system, Ornstein-Uhlenbeck (OU) processes have been used, usually replacing the body-fixed constant velocity with a noisy velocity performing an OU process around a body-fixed average [50]. An OU process is Brownian motion confined by a harmonic potential, such that the potential minimum defines the average. The decay time to reach this average defines a timescale; thus, it effectively corresponds to colored noise. In recent years, the OU process has been extensively used to model the stochastic motion of 2D swimmers [51–58]. However, the approach of using an OU process has not yet been explicitly extended to chiral particles in 3D, although earlier work addressed a general case of time-correlated noise with arbitrary power spectrum [46]. This approach formally includes OU processes as special case, but this had not been worked out explicitly before (see below).

Here, we introduce a three-dimensional model which represents the noise in the generation of torque as an OU process, similarly as suggested previously for 2D [38]. This introduces a finite correlation time, reflecting transient but slower additional processes in the torque-generation mechanism, in contrast to uncorrelated (white) Brownian noise. Analyzing the gliding of the malaria parasites through hydrogels as visualized in Fig. 1(a) (see Appendix A for details), we found that the typical turning time is 22 s and that the correlation of the direction of the angular velocity decays with two clearly separated timescales; compare Fig. 1(b). The large timescale of 100 s is much larger than the turning time and, thus, corresponds to

the decay of orientation of the centerline of the helix, which is the global feature of a helical motion. By contrast, the small timescale of 20 s must then correspond to more local features in time, in particular, to the correlation time of the force-generating processes. The internal correlation time likely results from reorientation in the flow field of the adhesins on the parasite surface, which earlier has been shown both experimentally and theoretically to be very variable and to self-organize for productive gliding [16,59].

As we demonstrate here, our 3D OU model for chiral active particles can be treated analytically by suitably truncating a hierarchy of equations. We derive equations for the effective correlation time, the mean position, and the mean squared displacement (MSD). Our main finding is that, in 3D, chirality and, hence, rotation can lead to enhanced effective persistence compared to nonrotating particles by an integrative effect of stochastic noise—a stabilization that can even lead to helical trajectories becoming "straighter than a straight line," i.e., allowing for larger long-time MSD compared to a particle moving with the same speed on a straight trajectory without rotation. A similar conclusion has been drawn before from computer simulations of swimming sperm [49]. This suggests that helical trajectories are favored for microorganisms that have to quickly move large distances through their environment. Finally, we compare our model to experimental data from malaria parasites, demonstrating that it can describe the experimentally observed large MSD.

Model—The overdamped motion of swimming and gliding microorganisms can be effectively characterized by translational and angular velocities. This is equivalent to a description in terms of active forces and torques for gliding microorganisms [16] and has been used before also for asymmetric low Reynolds number microswimmers [32]. To model the intrinsic rotational noise, we consider an active particle that is moving with a body-fixed constant translational velocity $\mathbf{V}_0^{\text{body}}$. Its rotational velocity performs an OU process around the body-fixed average $\mathbf{\Omega}_0^{\text{body}}$. In the lab frame, we use two vectors to track the orientation of the particle. $\mathbf{n}_1$ is the direction of the mean angular velocity $\mathbf{\Omega}_0$, and $\mathbf{n}_2 \perp \mathbf{n}_1$ is defined with the angle α between $\mathbf{\Omega}_0$ and $\mathbf{V}_0$ (see Fig. 6 in Appendix A):

$$\mathbf{\Omega}_0 = \Omega_0 \mathbf{n}_1, \qquad \mathbf{V}_0 = |\mathbf{V}_0|(\mathbf{n}_1 \cos\alpha + \mathbf{n}_2 \sin\alpha). \quad (1)$$

For simplicity, we set $|\mathbf{V}_0| = 1$ in the following. In the lab frame, the equations of motion are

$$d\mathbf{\Omega} = -k(\mathbf{\Omega} - \Omega_0 \mathbf{n}_1)dt + h\,d\mathbf{\Lambda}, \quad (2)$$

$$d\mathbf{n}_1 = (\mathbf{\Omega} \times \mathbf{n}_1)dt, \quad (3)$$

$$d\mathbf{n}_2 = (\mathbf{\Omega} \times \mathbf{n}_2)dt, \quad (4)$$

$$d\mathbf{r} = (\cos(\alpha)\mathbf{n}_1 + \sin(\alpha)\mathbf{n}_2)dt. \quad (5)$$

Here, k is the potential strength and h the noise amplitude of the OU process. $d\Lambda$ is a 3D standard Wiener process. Note that noise is not multiplicative in the lab frame. Focusing on the intrinsic noise for simplicity, we disregard external noise (such as Brownian translational noise) or intrinsic noise in the translational velocity.

Rotation—The rotational part described by Eqs. (2) and (3) is decoupled from the rest and can be solved first. The dynamical equations for the expectation values $\langle \mathbf{\Omega} \rangle$ and $\langle \mathbf{n}_1 \rangle$ constitute an infinite hierarchy of expectation values of cross products of these two quantities, the first four being $\langle \mathbf{\Omega} \rangle$, $\langle \mathbf{n}_1 \rangle$, $\langle \mathbf{\Omega} \times \mathbf{n}_1 \rangle$, and $\langle \mathbf{\Omega} \times (\mathbf{\Omega} \times \mathbf{n}_1) \rangle$. We can apply moment closure to the higher-order terms in the dynamic equation for $\langle \mathbf{\Omega} \times (\mathbf{\Omega} \times \mathbf{n}_1) \rangle$ to truncate this hierarchy (see Appendix B).

By rotational symmetry, only the component singled out by the initially parallel $\mathbf{\Omega}$ and $\mathbf{n}_1$ axes is relevant (as the rotational problem is independent of $\mathbf{n}_2$), and the other two components of each vector vanish upon averaging (we choose this direction to be z). Hence, the truncated system defines a four-dimensional, linear, homogeneous ordinary differential equation problem, which we can analyze by its eigenvalues.

The mode relevant for the long-time behavior can be identified as the unique mode with real eigenvalue and parallel $\langle \mathbf{\Omega} \rangle$ and $\langle \mathbf{n}_1 \rangle$, which describes the decorrelation of $\langle \mathbf{\Omega} \rangle$ from its initial orientation. The other eigenvalues describe the unstable state where $\mathbf{\Omega}$ and $\mathbf{n}_1$ are antiparallel, and oscillatory states, all of which decay more quickly. The relevant eigenvalue can be computed exactly but is cumbersome as a solution of a fourth-order polynomial. Expanding for small k/Ω_0, i.e., assuming the rotation is faster then the timescale on which the OUP returns to its average, we get the approximation

$$\lambda = -\frac{h^2 + \Omega_0^2 k + k^3 - \sqrt{k^2(\Omega_0^2 + k^2)^2 - h^4}}{\Omega_0^2 + k^2}, \quad (6)$$

which describes the decay as $\langle \mathbf{\Omega} \rangle = (0, 0, \Omega_0) \exp(\lambda t)$ and $\langle \mathbf{n}_1 \rangle = (0, 0, 1) \exp(\lambda t)$. The more negative λ, the faster $\mathbf{\Omega}$ and $\mathbf{n}_1$ decorrelate from their initial orientation. For fixed noise amplitude h, both decreasing the strength k of the OUP potential and decreasing angular speed Ω_0 lead to faster decorrelation, suggesting that the rotation has a stabilizing effect. In the limits of vanishing noise, diverging potential strength, or diverging angular speed, the timescale of decorrelation diverges. In the limit of small noise amplitude, λ converges to the power spectrum of the OU process evaluated at the angular speed, consistent with a derivation starting from power spectra ([46]; see Supplemental Note 1 [60]).

To validate our approximations, we compared the solutions against numerical simulations of the initial model [Eqs. (2)–(5), implemented in JAX [66] using standard solvers for stochastic differential equations, set up in
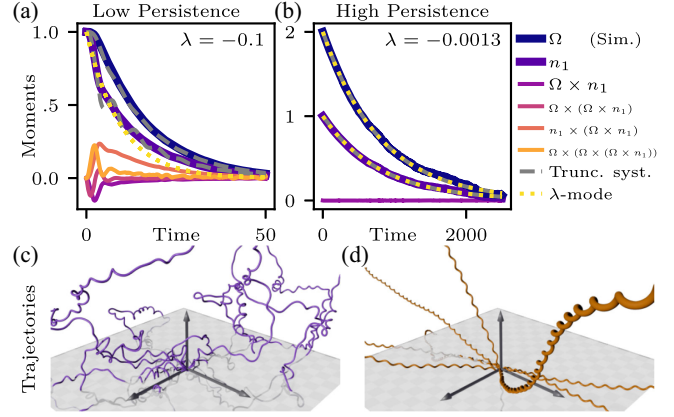

FIG. 2. (a) Time course of different moments obtained from numerical simulation [Eqs. (2)–(5)] in comparison with numerical solution of the truncated system [Eqs. (B1)–(B4), gray dashed lines] and analytical approximation predicting exponential decay with eigenvalue λ [Eq. (6), yellow dotted lines]. Parameter values: potential strength $k = 0.2$, noise amplitude $h = 0.3$, angular speed $\Omega_0 = 1$, and angle $\alpha = \pi/6$. (b) The same as (a), but now for $k = 2$, $h = 0.1$, and $\Omega_0 = 2$, i.e., much reduced noise and faster turning. Here, the agreement between simulations and theory is even better. (c) Simulated trajectories at parameters from (a). (d) Simulated trajectories at parameters from (b). The reduced noise leads to more regular trajectories. See also Supplemental Movies 1 and 2 [60].

DIFFRAX [67], and made publicly available [68]]. In Fig. 2, different expectation values obtained from averaging 20 000 numerical simulations are compared with (i) the numerically solved truncated ODE system [Eqs. (B1)–(B4), dashed gray line] and (ii) the analytical exponential decay given by the dominant eigenvalue λ. As shown in Fig. 2(a), larger noise yielding faster decorrelation produces larger values of the higher-order expectation values. We find that the truncations are qualitatively correct (see also Supplemental Fig. S1 [60]), while quantitative differences are visible—the numerical solution of the truncated system shows some additional oscillations. The exponential decay by λ is too fast here, which signifies that during the relatively rapid decay, additional modes are relevant. For lower noise, in Fig. 2(b) we see excellent agreement between numerical simulation, numerical solution of the truncated system, and the exponential decay given by λ from Eq. (6). The latter decay completely dictates the persistence in the resulting motion, as also apparent in the resulting trajectories illustrated in Figs. 2(c) and 2(d). Generally, lower decorrelation can be reached by lower noise amplitude h, stronger Ornstein-Uhlenbeck potential k, or higher angular speed Ω_0.

Translation—For the analytical treatment of the translational part, we assume that initially $\mathbf{\Omega} = \Omega_0 \mathbf{n}_1$ is in the z direction. The solution of the rotational part then allows one to solve Eq. (5) for the motion in z, $d\langle z \rangle = \cos(\alpha) \langle \mathbf{n}_1 \rangle$. To obtain the MSD and the remaining coordinates, we need an expression for $\langle \mathbf{n}_2 \rangle$. By construction, $\mathbf{n}_2 \perp \mathbf{n}_1$, so $\mathbf{n}_2$ is

rotating in the plane perpendicular to $\mathbf{n}_1$ with angular frequency Ω_0, which is on average the x-y plane. We assume that $\mathbf{n}_2$ initially points in the x direction. The decorrelation of $\mathbf{n}_1$ is also decorrelating the plane in which $\mathbf{n}_2$ rotates, but the latter additionally decorrelates within the plane by variations of the magnitude of the rotational velocity. Both effects are caused by $\mathbf{\Omega}$ deviating from $\mathbf{\Omega}_0$, the tilting of the plane by deviations perpendicular to $\mathbf{\Omega}_0$, and in-plane deviations by parallel components. Because of this additional effect, we obtain a twofold faster decorrelation of $\langle \mathbf{n}_2 \rangle$ compared to $\langle \mathbf{n}_1 \rangle$ (see Supplemental Note 2 [60]):

$$\langle \mathbf{n}_2 \rangle = (\cos \Omega_0 t, \sin \Omega_0 t, 0) e^{2\lambda t}. \quad (7)$$

The MSD can now be obtained (see Appendix C) by first computing it from the formal solution and inserting the solutions obtained for $\langle \mathbf{n}_1 \rangle$ and $\langle \mathbf{n}_2 \rangle$. The result is (except for the degenerate case $\Omega_0 = 0$ and $\alpha > 0$)

$$
\begin{aligned}
\langle \mathbf{r}_{(t)}^2 \rangle = {} & \frac{2\cos^2(\alpha)(-\lambda t + e^{\lambda t} - 1)}{\lambda^2} \\
& + \frac{2\sin^2(\alpha)}{(4\lambda^2 + \Omega_0^2)^2} [-4\lambda^2 + \Omega_0^2 - 2\lambda(4\lambda^2 + \Omega_0^2)t \\
& + (4\lambda^2 - \Omega_0^2) e^{2\lambda t} \cos(\Omega_0 t) + 4\lambda\Omega_0 e^{2\lambda t} \sin(\Omega_0 t)].
\end{aligned}
\quad (8)
$$

Let us consider two limiting cases. First, for $\alpha = 0$, corresponding to a particle rotating while traveling in average on a straight line, we obtain

$$\langle \mathbf{r}_{(t)}^2 \rangle = -\frac{2}{\lambda} t - \frac{2}{\lambda^2} (1 - e^{\lambda t}), \quad (9)$$

which recovers the case of an active Brownian particle (see Supplemental Note 1 [60]; note $\lambda < 0$). Second, for general α in the limit of large t, we can approximate $\langle \mathbf{r}_{(t)}^2 \rangle \approx 6D_\infty t$, where we obtain the effective diffusion constant describing the long-time behavior as

$$D_\infty = -\frac{\lambda}{3} \left(\frac{\cos^2(\alpha)}{\lambda^2} + \frac{2\sin^2(\alpha)}{(4\lambda^2 + \Omega_0^2)} \right). \quad (10)$$

In the case $\lambda^2 \ll \Omega_0^2$, meaning small noise leading to a decay time much longer than the rotation period, and $\alpha < \pi/2$, i.e., the particle not just circling, but having some average net movement, this reduces to $D_\infty \approx -\cos^2(\alpha)/(3\lambda)$.

Lastly, with Eq. (7) we compute $\langle x \rangle$ and $\langle y \rangle$ by integrating $d\langle x \rangle = \sin(\alpha) \langle \mathbf{n}_2 \rangle_x dt$, allowing us to obtain the expectation value of the trajectory:

$$
\langle \mathbf{r}_{(t)} \rangle = \begin{pmatrix} \sin(\alpha) \frac{e^{2\lambda t}[2\lambda \cos(\Omega_0 t) + \Omega_0 \sin(\Omega_0 t)] - 2\lambda}{4\lambda^2 + \Omega_0^2} \\ \sin(\alpha) \frac{e^{2\lambda t}[2\lambda \sin(\Omega_0 t) - \Omega_0 \cos(\Omega_0 t)] + \Omega_0}{4\lambda^2 + \Omega_0^2} \\ \frac{\cos(\alpha)}{\lambda} (e^{\lambda t} - 1) \end{pmatrix}, \quad (11)
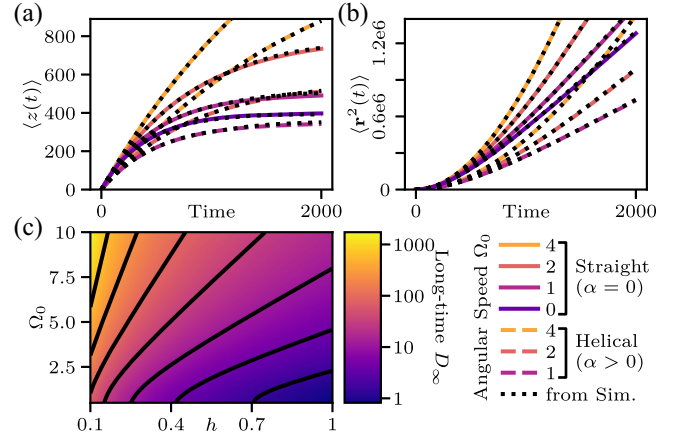$$

FIG. 3. (a) Mean distance traveled in the z direction (the initial orientation of the helical axis) for different Ω_0 at $k = 2$, $h = 0.1$. Full lines show particles moving straight while turning ($\alpha = 0$), dashed lines particles on helical trajectories ($\alpha = \pi/4$), which can be seen overtaking slower turning straight particles. Colored and black lines are theoretical and numerical, respectively, and in very good agreement. (b) Mean squared displacement for the same parameters as shown in (a), theoretical results from Eq. (8) in color. (c) Effective long-time diffusion constant D_∞ [cf. Eq. (10)] as a function of noise amplitude h and angular speed Ω_0. Black lines mark contours of constant D_∞.

which is a logarithmic spiral on a radical surface, i.e., $z \propto \sqrt{r}$.

Results—The derived solutions show that increasing rotation Ω_0 stabilizes the particle against its intrinsic noise. In Figs. 3(a) and 3(b), we plot the mean z position and the MSD, respectively, which both increase with increasing angular speed. In both cases, we find that the numerical simulations [68] agree well with the analytical results; cf. Eq. (8) and the third component of Eq. (11). The plots show that if the particle travels on a helix [case $\alpha = \pi/4$; cf. dashed lines in Figs. 3(a) and 3(b)] with the same speed as a nonrotating particle traveling in a straight fashion, if it turns sufficiently fast (i.e., if the angular velocity Ω_0 is sufficiently large), it travels further from the origin on average at large timescales. Therefore, a helical trajectory can be "straighter than a straight line."

The long-time behavior is described by the effective diffusion constant Eq. (10), which has a complicated dependence on Ω_0, k, and h through λ. In Fig. 3(c), we see that, at constant OU potential strength k, D_∞ increases with higher angular speed Ω_0, as this suppresses deviations of the helical axis, different from what was found for chiral active Brownian particles without the OU process [48] (see Supplemental Note 1 [60]). This effect becomes more pronounced for higher noise amplitude h; i.e., at higher noise, the stabilizing effect of rotation is more pronounced. Increasing effective diffusion by introducing rotation or, equivalently, chirality is strikingly different from known examples. In 2D, chirality reduces long-time diffusion by enforcing circular turning [34,69]. Similarly, a 3D active
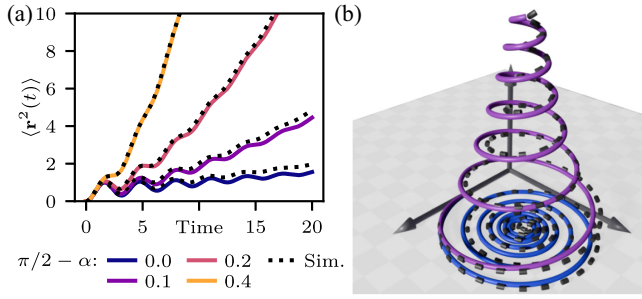
FIG. 4. (a) Mean squared displacement for α close to $\pi/2$, such that the particles are close to describing circles, with $k = 1$, $h = 0.5$, and $\Omega_0 = 2$. Black dotted lines are averages from numerical simulations. (b) Theoretical expectation value of trajectories [Eq. (11)] for the two lower values of $\pi/2 - \alpha$.

Brownian particle with external torque exhibits reduced long-time diffusion [27].

We can also study the short-time behavior. Figure 4(a) shows that, at short times, the MSD of a helix grows slower, because it is curving back onto itself, depending on the pitch of the helix defined by the angle α. For $\alpha = \pi/2$, the MSD shows strong oscillations, as the mean position [see Fig. 4(b)] describes a planar inward spiral due to the influence of noise that diverts it from the circle of a noise-free particle. For smaller α, the spiral gets the 3D structure of a logarithmic spiral on a radical surface as found in Eq. (11), with both cases showing good agreement between the numerical and analytical results (a similar spiral was found numerically in [47] for active Brownian particles with torque; see Supplemental Note 1 [60]).

Finally, we can use our measured trajectories for malaria parasites in hydrogels to extract their MSD [Fig. 5(a), averaged from 140 trajectories] and fit it with our model
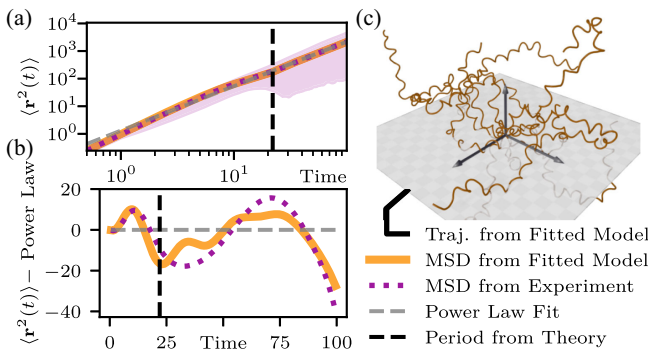

FIG. 5. (a) Log-log plot of the mean squared displacement extracted from observed malaria parasite trajectories shown in Fig. 1 (purple, dotted line), with five percent percentiles (purple, shaded) and the fitted model (orange line). The gray dashed line is a fitted power law. (b) Deviation from fitted power law. The vertical dashed line marks one period of rotation as extracted from the fitted model. (c) Trajectories simulated with parameters obtained from MSD fit resembling Fig. 1 (cf. Supplemental Movie 3 [60]).

prediction of Eq. (8), similar to what has been done before in 2D projections for choanoflagellate colonies [48]. In general, we find good agreement. Our theory successfully describes the first two extrema in the deviation of the MSD from a power law [Fig. 5(b)], corresponding to the first turn of the helix. Our theory also predicts some effects of second and third turns visible in the MSD deviation, which are not observable in the experimental data, most likely because the biological population has a distribution of helical pitches and radii such that the later turns cannot be resolved in the average. From the fitted model parameters (Appendix A), we can derive estimates for pitch and radius of the helical trajectories as 13.2 and 2.8 µm, respectively, well within the observed range [14]. We note in passing that a phenomenological fit of the period as the period in the MSD deviation would yield incorrect results for the oscillation period. Trajectories simulated with the fitted parameters [Fig. 5(c)] visually resemble the observed trajectories from Fig. 1.

In summary, our results suggest that helical trajectories provide an advantage for swimming or gliding microorganisms with noisy force generation to effectively cover distance more quickly than when going straight. This result from a general stochastic theory for microorganisms with colored noise in their internal torque generation complements early insight about the potential evolutionary advantages of helical motion for swimming [45,48,49]. Our results should apply also to cases of microswimmers with large internal correlation times, like the case of *Chlamydomonas* [70]. In general, it would be highly interesting to correlate measured correlation times with motion patterns and to interpret them in their ecological and evolutionary contexts. In the future, our model could also guide the design of micro- and nanobots [71,72], for example, in medical applications where enhanced persistence of motion is required [73].

Data availability—The data that support the findings of this article are openly available [68].

[1] J. G. Mitchell and K. Kogure, Bacterial motility: Links to the environment and a driving force for microbial physics, FEMS Microbiol. Ecol. **55**, 3 (2006).

[2] J. M. Keegstra, F. Carrara, and R. Stocker, The ecological roles of bacterial chemotaxis, Nat. Rev. Microbiol. **20**, 491 (2022).

[3] K. F. Jarrell and M. J. McBride, The surprisingly diverse ways that prokaryotes move, Nat. Rev. Microbiol. **6**, 466 (2008).

[4] U. S. Schwarz, Physical constraints for pathogen movement, Semin. Cell Dev. Biol. 46, 82 (2015).

[5] D. B. Kearns, A field guide to bacterial swarming motility, Nat. Rev. Microbiol. 8, 634 (2010).

[6] R. G. Douglas, R. W. Moon, and F. Frischknecht, Cytoskeleton organization in formation and motility of apicomplexan parasites, Annu. Rev. Microbiol. 78, 311 (2024).

[7] H. S. Jennings, On the significance of the spiral swimming of organisms, Am. Nat. 35, 369 (1901).

[8] H. C. Crenshaw, A new look at locomotion in microorganisms: Rotating and translating, Am. Zool. 36, 608 (1996).

[9] H. C. Berg and L. Turner, Chemotaxis of bacteria in glass capillary arrays. *Escherichia coli*, motility, microchannel plate, and light scattering, Biophys. J. 58, 919 (1990).

[10] R. Thar and T. Fenchel, True chemotaxis in oxygen gradients of the sulfur-oxidizing bacterium *Thiovulum majus*, Appl. Environ. Microbiol. 67, 3299 (2001).

[11] T. Fenchel and N. Blackburn, Motile chemosensory behaviour of phagotrophic protists: Mechanisms for and efficiency in congregating at food patches, Protistologica 150, 325 (1999).

[12] G. Jékely, J. Colombelli, H. Hausen, K. Guy, E. Stelzer, F. Nédélec, and D. Arendt, Mechanism of phototaxis in marine zooplankton, Nature (London) 456, 395 (2008).

[13] K. C. Leptos, M. Chioccioli, S. Furlan, A. I. Pesci, and R. E. Goldstein, Phototaxis of *Chlamydomonas* arises from a tuned adaptive photoresponse shared with multicellular volvocine green algae, Phys. Rev. E 107, 014404 (2023).

[14] J. Ripp, J. Kehrer, X. Smyrnakou, N. Tisch, J. Tavares, R. Amino, C. Ruiz de Almodovar, and F. Frischknecht, Malaria parasites differentially sense environmental elasticity during transmission, EMBO Mol. Med. 13, e13933 (2021).

[15] Z. Liu, S. Li, P. Anantha, T. Thanakornsombut, L. Wu, J. Chen, R. Tsuchiya, A. K. Tripathi, Y. Chen, and I. Barman, Plasmodium sporozoite shows distinct motility patterns in responses to three-dimensional environments, iScience 27, 110463 (2024).

[16] L. Lettermann, F. Ziebert, and U. S. Schwarz, A geometrical theory of gliding motility based on cell shape and surface flow, Proc. Natl. Acad. Sci. U.S.A. 121, e2410708121 (2024).

[17] H. C. Berg and E. M. Purcell, Physics of chemoreception, Biophys. J. 20, 193 (1977).

[18] H. C. Berg, *Random Walks in Biology* (Princeton University Press, Princeton, NJ, 1993).

[19] O. Pohl, M. Hintsche, Z. Alirezaeizanjani, M. Seyrich, C. Beta, and H. Stark, Inferring the chemotactic strategy of *P. putida* and *E. coli* using modified Kramers-Moyal coefficients, PLoS Comput. Biol. 13, e1005329 (2017).

[20] P. Romanczuk, M. Bär, W. Ebeling, B. Lindner, and L. Schimansky-Geier, Active Brownian particles, Eur. Phys. J. Special Topics 202, 1 (2012).

[21] C. Bechinger, R. Di Leonardo, H. Löwen, C. Reichhardt, G. Volpe, and G. Volpe, Active particles in complex and crowded environments, Rev. Mod. Phys. 88, 045006 (2016).

[22] A. Zöttl and H. Stark, Emergent behavior in active colloids, J. Phys. Condens. Matter 28, 253001 (2016).

[23] B. Liebchen and D. Levis, Chiral active matter, Europhys. Lett. 139, 67001 (2022).

[24] J. R. Howse, R. A. L. Jones, A. J. Ryan, T. Gough, R. Vafabakhsh, and R. Golestanian, Self-motile colloidal particles: From directed propulsion to random walk, Phys. Rev. Lett. 99, 048102 (2007).

[25] D. Debnath, P. K. Ghosh, Y. Li, F. Marchesoni, and B. Li, Diffusion of eccentric microswimmers, Soft Matter 12, 2017 (2016).

[26] J. R. Gomez-Solano, A. Blokhuis, and C. Bechinger, Dynamics of self-propelled Janus particles in viscoelastic fluids, Phys. Rev. Lett. 116, 138301 (2016).

[27] F. J. Sevilla, Diffusion of active chiral particles, Phys. Rev. E 94, 062120 (2016).

[28] J. R. Gomez-Solano and F. J. Sevilla, Active particles with fractional rotational Brownian motion, J. Stat. Mech. (2020) 063213.

[29] A. R. Sprenger, L. Caprini, H. Löwen, and R. Wittmann, Dynamics of active particles with translational and rotational inertia, J. Phys. Condens. Matter 35, 305101 (2023).

[30] S. van Teeffelen and H. Löwen, Dynamics of a Brownian circle swimmer, Phys. Rev. E 78, 020101(R) (2008).

[31] R. Ledesma-Aguilar, H. Löwen, and J. M. Yeomans, A circle swimmer at low Reynolds number, Eur. Phys. J. E 35, 70 (2012).

[32] F. Kümmel, B. ten Hagen, R. Wittkowski, I. Buttinoni, R. Eichhorn, G. Volpe, H. Löwen, and C. Bechinger, Circular motion of asymmetric self-propelling particles, Phys. Rev. Lett. 110, 198302 (2013).

[33] N. A. Marine, P. M. Wheat, J. Ault, and J. D. Posner, Diffusive behaviors of circle-swimming motors, Phys. Rev. E 87, 052305 (2013).

[34] H. Löwen, Chirality in microswimmer motion: From circle swimmers to active turbulence, Eur. Phys. J. Special Topics 225, 2319 (2016).

[35] A. Nourhani, S. J. Ebbens, J. G. Gibbs, and P. E. Lammert, Spiral diffusion of rotating self-propellers with stochastic perturbation, Phys. Rev. E 94, 030601(R) (2016).

[36] L. Caprini, H. Löwen, and U. M. B. Marconi, Chiral active matter in external potentials, Soft Matter 19, 6234 (2023).

[37] B. Lindner, Diffusion of particles subject to nonlinear friction and a colored noise, New J. Phys. 12, 063026 (2010).

[38] C. Weber, P. K. Radtke, L. Schimansky-Geier, and P. Hänggi, Active motion assisted by correlated stochastic torques, Phys. Rev. E 84, 011132 (2011).

[39] P. K. Ghosh, Y. Li, G. Marchegiani, and F. Marchesoni, Communication: Memory effects and active Brownian diffusion, J. Chem. Phys. 143, 211101 (2015).

[40] N. Narinder, C. Bechinger, and J. R. Gomez-Solano, Memory-induced transition from a persistent random walk to circular motion for achiral microswimmers, Phys. Rev. Lett. 121, 078003 (2018).

[41] P. Bayati and A. Nourhani, Memory effects in spiral diffusion of rotary self-propellers, Phys. Rev. E 105, 024606 (2022).

[42] A. R. Sprenger, S. Jahanshahi, A. V. Ivlev, and H. Löwen, Time-dependent inertia of self-propelled particles: The Langevin rocket, Phys. Rev. E 103, 042601 (2021).

[43] A. D. Rutenberg, A. J. Richardson, and C. J. Montgomery, Diffusion of asymmetric swimmers, Phys. Rev. Lett. 91, 080601 (2003).

[44] N. B. Becker and R. Everaers, From rigid base pairs to semiflexible polymers: Coarse-graining DNA, Phys. Rev. E 76, 021923 (2007).

[45] B. M. Friedrich and F. Jülicher, The stochastic dance of circling sperm cells: Sperm chemotaxis in the plane, New J. Phys. 10, 123025 (2008).

[46] B. M. Friedrich and F. Jülicher, Steering chiral swimmers along noisy helical paths, Phys. Rev. Lett. 103, 068102 (2009).

[47] R. Wittkowski and H. Löwen, Self-propelled Brownian spinning top: Dynamics of a biaxial swimmer at low Reynolds numbers, Phys. Rev. E 85, 021406 (2012).

[48] J. B. Kirkegaard, A. O. Marron, and R. E. Goldstein, Motility of colonial choanoflagellates and the statistics of aggregate random walkers, Phys. Rev. Lett. 116, 038102 (2016).

[49] X. Ren and H. Bloomfield-Gadêlha, Swimming by spinning: Spinning-top type rotations regularize sperm swimming into persistently progressive paths in 3d, Adv. Sci. 12, 2406143 (2025).

[50] G. Szamel, Self-propelled particle in an external potential: Existence of an effective temperature, Phys. Rev. E 90, 012111 (2014).

[51] F. J. Sevilla, R. F. Rodríguez, and J. R. Gomez-Solano, Generalized Ornstein-Uhlenbeck model for active motion, Phys. Rev. E 100, 032123 (2019).

[52] E. Woillez, Y. Kafri, and V. Lecomte, Nonlocal stationary probability distributions and escape rates for an active Ornstein–Uhlenbeck particle, J. Stat. Mech. (2020) 063204.

[53] D. Martin, J. O'Byrne, M. E. Cates, E. Fodor, C. Nardini, J. Tailleur, and F. van Wijland, Statistical mechanics of active Ornstein-Uhlenbeck particles, Phys. Rev. E 103, 032607 (2021).

[54] D. Martin and T. A. d. Pirey, AOUP in the presence of Brownian noise: A perturbative approach, J. Stat. Mech. (2020) 043205.

[55] G. H. P. Nguyen, R. Wittmann, and H. Löwen, Active Ornstein–Uhlenbeck model for self-propelled particles with inertia, J. Phys. Condens. Matter 34, 035101 (2021).

[56] A. Crisanti and M. Paoluzzi, Most probable path of active Ornstein-Uhlenbeck particles, Phys. Rev. E 107, 034110 (2023).

[57] S. Dutta, Most probable paths for active Ornstein-Uhlenbeck particles, Phys. Rev. E 107, 054130 (2023).

[58] J. H. Fritz and U. Seifert, Thermodynamically consistent model of an active Ornstein–Uhlenbeck particle, J. Stat. Mech. (2023) 093204.

[59] C. L. Hueschen, L.-A. Segev-Zarko, J.-H. Chen, M. A. LeGros, C. A. Larabell, J. C. Boothroyd, R. Phillips, and A. R. Dunn, Emergent actin flows explain distinct modes of gliding motility, Nat. Phys. 20, 1989 (2024).

[60] See Supplemental Material at http://link.aps.org/supplemental/10.1103/4kxb-h6p4, which includes a detailed comparison of the active Ornstein-Uhlenbeck particle with other models (Note 1), two supplemental figures illustrating these comparisons, a more technical part of the derivations (Note 2), and captions for the supplemental videos. It also includes Refs. [61–65].

[61] O. Kratky and G. Porod, Röntgenuntersuchung gelöster fadenmoleküle, Recl. Trav. Chim. Pays-Bas 68, 1106 (1949).

[62] M. Doi, S. F. Edwards, and S. F. Edwards, The Theory of Polymer Dynamics (Oxford University Press, New York, 1988), Vol. 73.

[63] C. W. Gardiner, Handbook of Stochastic Methods for Physics, Chemistry and the Natural Sciences, Springer Series in Synergetics (ACS Publications, Washington D.C., 1985).

[64] P. Hänggi and P. Jung, Colored noise in dynamical systems, Adv. Chem. Phys. 89, 239 (1994).

[65] R. N. Bhattacharya, On the functional central limit theorem and the law of the iterated logarithm for Markov processes, Z. Wahrscheinlichkeitstheorie Verw. Geb. 60, 185 (1982).

[66] J. Bradbury, R. Frostig, P. Hawkins, M. J. Johnson, C. Leary, D. Maclaurin, G. Necula, A. Paszke, J. VanderPlas, S. Wanderman-Milne, and Q. Zhang, JAX: Composable transformations of Python+NumPy programs (2018).

[67] P. Kidger, On neural differential equations, Ph.D. thesis, University of Oxford, 2021.

[68] Repository containing Python code for the simulations and analytical solutions, https://github.com/LeonLettermann/3D-Chiral-OUP.

[69] K. S. Olsen and H. Löwen, Optimal diffusion of chiral active particles with strategic reorientations, Phys. Rev. E 110, 064606 (2024).

[70] K. Y. Wan and R. E. Goldstein, Rhythmicity, recurrence, and recovery of flagellar beating, Phys. Rev. Lett. 113, 238103 (2014).

[71] A. Ghosh and P. Fischer, Controlled propulsion of artificial magnetic nanostructured propellers, Nano Lett. 9, 2243 (2009).

[72] T. Yamamoto and M. Sano, Chirality-induced helical self-propulsion of cholesteric liquid crystal droplets, Soft Matter 13, 3328 (2017).

[73] J. Llacer-Wintle, A. Rivas-Dapena, X.-Z. Chen, E. Pellicer, B. J. Nelson, J. Puigmartí-Luis, and S. Pané, Biodegradable small-scale swimmers for biomedical applications, Adv. Mater. 33, 2102049 (2021).

[74] J. M. Leung, M. A. Rould, C. Konradt, C. A. Hunter, and G. E. Ward, Disruption of TgPHIL1 alters specific parameters of Toxoplasma gondii motility measured in a quantitative, Three-dimensional live motility assay, PLoS One 9, e85763 (2014).

End Matter

Appendix A: Experimental details—Malaria is caused by unicellular parasites of the genus *Plasmodium*. During its complex life cycle, the sporozoite, a 10-μm-long, crescent-shaped motile stage of the parasite, is transmitted from a mosquito during its blood meal and utilizes rapid gliding motility to migrate in the skin to enter blood vessels. The experimental setup [14] consists of a soft and porous polyacrylamide hydrogel serving as

TABLE I. Results for fitting the model to the MSD computed from experimentally observed and resampled trajectories of malaria parasites.

Parameter	Ω_0	α	k	h
Fit result	0.285 1/s	0.926	1.078 1/s	0.154 $1/s^{3/2}$

3D substrate mimicking the host skin. A mosquito salivary gland infected by *P. berghei* sporozoites that express a fluorescent protein in their cytoplasm was placed on top of the gel, such that sporozoites could invade into the gel at high numbers. 3D sporozoite migration was observed using spinning disk confocal microscopy, which allowed us to follow the rapid migration of hundreds of parasites.

The microscopy results were processed by an automated image analysis pipeline. Standard filtering and registration approaches were combined with a custom-built deconvolution and tracking pipeline to obtain 3D trajectories of individual sporozoites.

Experimentally observed sporozoites do not move at a constant speed, and even their average speed can vary between different parasites by a factor of 3. For this analysis, we resampled the trajectories by fitting a Fourier series (similar to Ref. [74]) and assuming a constant speed of 1 μm/s. We used 140 trajectories with lengths between 100 and 300 μm. The fit of the MSD in Fig. 5 results in the parameters given in Table I.

To estimate the correlation timescale of the angular velocity, we can obtain the estimated vector $\mathbf{\Omega}_{(t)}$ from the trajectories as the Darboux vector of the Frenet frame, which can be derived from the fitted Fourier series. While the modulus shows a relatively noisy behavior, the direction decays on two clearly separated timescales as shown in
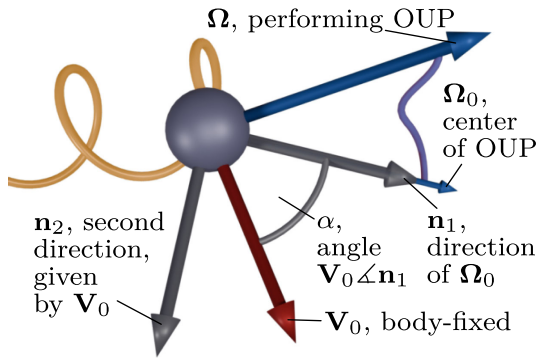
Fig. 7. The large timescale of $\tau \approx 100$ s describes the decorrelation of the helical axis. Additionally, a second, shorter timescale is visible, as expected from the Ornstein-Uhlenbeck process (Gaussian white noise would lead to decay with only a single timescale). This short timescale of $\tau = 20$ s represents the timescale on which the axis of rotation of the internal force generating apparatus fluctuates during motion. It is notably smaller than the timescale $1/k$ as extracted from the MSD fit, which would give the timescale of decay for the full $\mathbf{\Omega}$ in the OUP if $\mathbf{n}_1$ would be fixed. Note, however, that the direction of angular velocity $\mathbf{\Omega}/|\mathbf{\Omega}|$ relative to the moving center of the OUP follows a more complicated decay law. Additionally, it is likely that for the malaria parasite the assumed isotropy of the OUP is not exactly true, and the magnitude of the angular velocity fluctuates faster than the direction.

Appendix B: Moment closure of the rotational problem—The dynamic equations for the first four moments expanding the rotational problem [Eqs. (2) and (3)] are

$$d\langle\mathbf{\Omega}\rangle = -k(\langle\mathbf{\Omega}\rangle - \Omega_0\langle\mathbf{n}_1\rangle)dt, \tag{B1}$$

$$d\langle\mathbf{n}_1\rangle = \langle\mathbf{\Omega}\times\mathbf{n}_1\rangle dt, \tag{B2}$$

$$d\langle\mathbf{\Omega}\times\mathbf{n}_1\rangle = -k\langle\mathbf{\Omega}\times\mathbf{n}_1\rangle dt + \langle\mathbf{\Omega}\times(\mathbf{\Omega}\times\mathbf{n}_1)\rangle dt, \tag{B3}$$

and

$$\begin{aligned}
d\langle\mathbf{\Omega}\times(\mathbf{\Omega}\times\mathbf{n}_1)\rangle = &-2k\langle\mathbf{\Omega}\times(\mathbf{\Omega}\times\mathbf{n}_1)\rangle dt \\
&+ \langle\mathbf{\Omega}\times(\mathbf{\Omega}\times(\mathbf{\Omega}\times\mathbf{n}_1))\rangle dt \\
&+ k\Omega_0\langle\mathbf{n}_1\times(\mathbf{\Omega}\times\mathbf{n}_1)\rangle dt \\
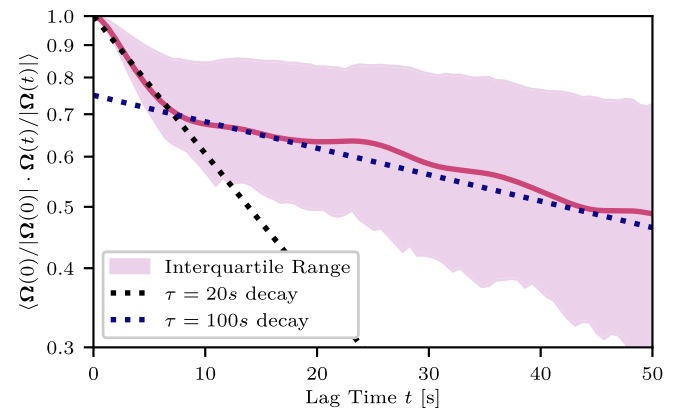&+ h^2\langle d\mathbf{\Lambda}\times(d\mathbf{\Lambda}\times\mathbf{n}_1)\rangle.
\end{aligned}$$

FIG. 6. Model schematics. The translational velocity $\mathbf{V}_0$ is fixed in the body frame, but the angular velocity $\mathbf{\Omega}$ performs an Ornstein-Uhlenbeck process (OUP) centered around the body fixed $\mathbf{\Omega}_0$. The body coordinates are given by the vectors $\mathbf{n}_1$, the direction of the average angular velocity $\mathbf{\Omega}_0$, and $\mathbf{n}_2$, chosen such that $\mathbf{V}_0$ is in the plane spanned by $\mathbf{n}_1$, $\mathbf{n}_2$, with an angle of α between $\mathbf{V}_0$ and $\mathbf{n}_1$. See also Supplemental Movies 1–3 [60].

FIG. 7. The autocorrelation of the normalized Darboux vector, $\langle\mathbf{\Omega}(0)/|\mathbf{\Omega}(0)|\cdot\mathbf{\Omega}(t)/|\mathbf{\Omega}(t)|\rangle$, as estimated from experimental trajectories, displays a decay of autocorrelation with a fast ($\tau = 20$ s) and a slow ($\tau = 100$ s) regime. The shaded area displays the 25%–75% interquartile range, and the solid line is the average.

To obtain an analytical solution, we apply moment closure by approximating the second and third terms in this equation. The truncation cannot be performed earlier due to the necessity of retaining terms up to second order in Ω to properly account for the effect of noise. First, assuming $\langle \Omega^2 A \rangle \approx \Omega_0^2 \langle A \rangle$, we get for the second term $\langle \Omega \times (\Omega \times (\Omega \times \mathbf{n}_1)) \rangle \approx -\Omega_0^2 \langle \Omega \times \mathbf{n}_1 \rangle$. For the third term, upon replacing Ω with $\Omega^\perp$, its component perpendicular to $\mathbf{n}_1$, the relevant contribution for the cross product, and applying similar logic as before but with $|\mathbf{n}_1| = 1$, we get $\langle \mathbf{n}_1 \times (\Omega \times \mathbf{n}_1) \rangle = \langle \Omega^\perp \rangle = \langle \Omega - (\Omega \cdot \mathbf{n}_1)\mathbf{n}_1 \rangle \approx \langle \Omega \rangle - \Omega_0 \langle \mathbf{n}_1 \rangle$. For the last approximation, we assumed that the variance of the OU process is small, such that Ω stays close to its average $\Omega_0 \mathbf{n}_1$. The noise term can be explicitly computed, and we can close the hierarchy by rewriting its fourth equation as

$$
\begin{aligned}
&\mathrm{d}\langle \Omega \times (\Omega \times \mathbf{n}_1) \rangle \\
&= -2k\langle \Omega \times (\Omega \times \mathbf{n}_1) \rangle \mathrm{d}t - \Omega_0^2 \langle \Omega \times \mathbf{n}_1 \rangle \mathrm{d}t \\
&\quad + k\Omega_0(\langle \Omega \rangle - \Omega_0 \langle \mathbf{n}_1 \rangle)\mathrm{d}t - 2h^2 \langle \mathbf{n}_1 \rangle \mathrm{d}t.
\end{aligned} \tag{B4}
$$

The truncation presented above breaks down for $\Omega_0 = 0$, because the equation for Ω decouples from the rest, and $\langle \Omega \rangle$ is dominated by the MSD of the OUP instead of Ω_0. However, in the limit of small noise ($h^2 \ll k^3$), the previously derived eigenvalue [Eq. (6)] has a well-defined limit

$$
\lambda|_{\Omega_0=0} \approx -\frac{h^2}{k^2}. \tag{B5}
$$

Following through the previous derivation of Eq. (B4) for the case of $\Omega_0 = 0$ and truncating $\langle \Omega \times (\Omega \times (\Omega \times \mathbf{n}_1)) \rangle \approx -h^2/(2k)\langle \Omega \times \mathbf{n}_1 \rangle$, using the MSD of the OUP instead of Ω_0^2, we find the same result. Therefore, even if the original derivation is not valid, the eigenvalue as written correctly includes the $\Omega_0 \to 0$ limiting case. This is also confirmed by the numerical simulations for the $\Omega_0 = 0$ case in Fig. 3.

Appendix C: Derivation of MSD—The MSD can now be obtained by first computing it from the formal solution

$$
\mathbf{r}_{(t)} = \int_0^t \mathrm{d}t(\cos(\alpha)\mathbf{n}_1 + \sin(\alpha)\mathbf{n}_2), \tag{C1}
$$

which yields

$$
\begin{aligned}
\langle \mathbf{r}_{(t)}^2 \rangle = \int_0^t \mathrm{d}s_1 \int_0^t \mathrm{d}s_2 (&\cos^2(\alpha)\langle \mathbf{n}_1(s_1) \cdot \mathbf{n}_1(s_2) \rangle \\
&+ \sin^2(\alpha)\langle \mathbf{n}_2(s_1) \cdot \mathbf{n}_2(s_2) \rangle),
\end{aligned} \tag{C2}
$$

where the mixed terms vanish, as due to their perpendicularity and the rotational symmetry the expectation value of their scalar products has to be zero even if evaluated at different times. The remaining correlation functions can be directly obtained from the solutions obtained for $\langle \mathbf{n}_1 \rangle$ and $\langle \mathbf{n}_2 \rangle$ as

$$
\langle \mathbf{n}_1(s_1) \cdot \mathbf{n}_1(s_2) \rangle = e^{\lambda|s_1 - s_2|}, \tag{C3}
$$

$$
\langle \mathbf{n}_2(s_1) \cdot \mathbf{n}_2(s_2) \rangle = \cos(\Omega_0|s_1 - s_2|)e^{2\lambda|s_1 - s_2|}, \tag{C4}
$$

such that we finally compute the MSD by simple integration.